Analysis of optical interferometric displacement detection in nanoelectromechanical systems

D. Karabacak, T. Kouh,[a] and K. L. Ekinci[b]
Aerospace and Mechanical Engineering Department, Boston University, Boston, Massachusetts 02215

Optical interferometry has found recent use in the detection of nanometer scale displacements of nanoelectromechanical systems (NEMS). At the reduced length scale of NEMS, these measurements are strongly affected by the diffraction of light. Here, we present a rigorous numerical model of optical interferometric displacement detection in NEMS. Our model combines finite element methods with Fourier optics to determine the electromagnetic field in the *near-field* region of the NEMS and to propagate this field to a detector in the *far field*. The noise analysis based upon this model allows us to elucidate the displacement sensitivity limits of optical interferometry as a function of device dimensions as well as important optical parameters. Our results may provide benefits for the design of next generation, improved optical NEMS. © *2005 American Institute of Physics*. [DOI: 10.1063/1.2148630]

I. INTRODUCTION

Submicron electromechanical devices are being developed for a variety of applications as well as for accessing interesting regimes of fundamental research.[1,2] These nanoelectromechanical systems (NEMS) have recently achieved fundamental resonance frequencies exceeding 1 GHz with quality (Q) factors in the $10^3 \leqslant Q \leqslant 10^5$ range.[3] Even at this early stage of their development, it seems clear that NEMS will find use in a broad range of applications. Recent demonstrations of NEMS-based electrometry,[4] optomechanical[5] and electromechanical[6] signal processing, and mass detection[7–10] have attracted much attention. From a fundamental science point of view, NEMS are opening up investigations of phonon-mediated mechanical processes[11,12] and of the quantum behavior of mesoscopic mechanical systems.[13,14]

One of the most important technological challenges in NEMS operation is the detection of subnanometer NEMS displacements at high (resonance) frequencies. Recently, optical interferometries, in particular, path-stabilized Michelson interferometry and Fabry-Perot interferometry, have been used to detect NEMS displacements at room temperature.[15–19] In path-stabilized Michelson interferometry, a tightly focused laser beam reflects from the surface of a NEMS device in motion and interferes with a reference beam. In the case of Fabry-Perot interferometry, the optical cavity formed within the sacrificial gap of a NEMS device—between the device surface and the substrate—modulates the optical signal on a photodetector as the structure moves in the out-of-plane direction. In both these techniques, strong diffraction effects emerge[19] as the relevant NEMS dimensions are reduced beyond the optical wavelength used. There

is a clear need to quantitatively understand the effects of such diffraction phenomena upon the sensitivity of nanoscale displacement detection.

Detailed theoretical models[20,21] have been developed to elucidate the displacement sensitivity of optical interferometry—albeit on objects with cross sections larger than the diffraction-limited optical spot. These models accurately describe the sensitivity limits, especially in atomic force microscopy[22–25] (AFM) and laser ultrasound[26] applications. There are several challenges in extending such models into the domain of NEMS. First, subwavelength NEMS sizes require the accurate solution of the electromagnetic (EM) field equations in the vicinity of the device. Second, due to the layered nature of most NEMS, the EM field travels in several different media, thus necessitating a careful consideration of material properties. Third, incorporation of the solutions in the device near field into a realistic model with a far-field detector is computationally intensive.

In this article, our main focus is to gain a quantitative understanding of the way optical interferometric displacement detection works in subwavelength NEMS. Several key elements ought to be considered: (a) the effective NEMS interaction with the EM field, (b) the propagation of the EM field to the detector, and (c) the detection of the optical signal via the photodetector circuitry. At the center of the approach presented here is a numerical analysis of the EM field in the vicinity of the NEMS. The EM field emerging from the numerical analysis is collimated and propagated in free space. Finally, the power in this field is converted into an electronic current. This formalism combining all the elements of optical detection facilitates a detailed noise analysis. For the noise analysis, we have investigated various noise sources, including both fundamental and experimental ones.

Even though our focus in this paper is upon establishing the limits to optical displacement detection in NEMS, the results we obtain are far more general. As discussed in more

[a]Present address: Department of Physics, Kookmin University, Seoul 136-702, Korea.
[b]Author to whom correspondence should be addressed; electronic mail: ekinci@bu.edu

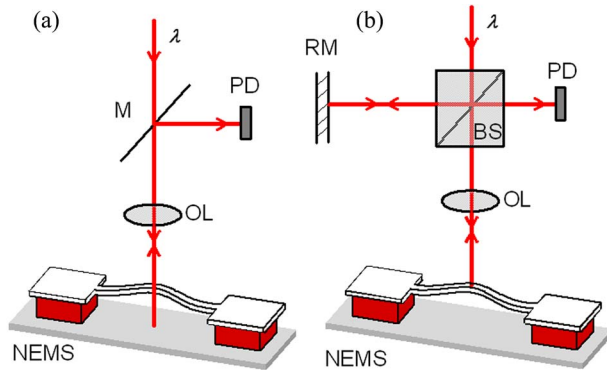**98**, 124309-1 © 2005 American Institute of Physics

FIG. 1. (Color online) Optical interferometric displacement detection in NEMS. A probing laser beam of wavelength λ is focused on the center of a doubly clamped beam through an objective lens (OL). (a) In Fabry-Perot interferometry, the reflected light from the NEMS structure is collimated through the same lens and is directed on to a photodetector (PD). (b) In Michelson interferometry, the light from the device interferes with a reference beam created using a reference mirror (RM) and a beam splitter (BS).

detail below, a crucial aspect of investigating the optical displacement sensitivity in NEMS is, in fact, determining the details of EM field diffraction by subwavelength NEMS. In this respect, our work is complementary to a recent work where the interaction of light with subwavelength structures has been studied. Such studies are becoming increasingly important[27,28] as in many emerging technologies, devices are being miniaturized.[29] Numerical analysis of such problems has been performed using a variety of methods, such as finite difference time domain (FDTD), finite difference frequency domain[29] (FDFD), and integral formulation.[27]

This paper is organized as follows. In Sec. II, we consider each component in the problem and develop a general approach to model the displacement sensitivity of optical interferometry in NEMS. Section III is dedicated to a study of the Fabry-Perot interferometry technique in multilayered NEMS using the developed model. In Sec. IV, the model is extended to analyze path-stabilized Michelson interferometry. In Sec. V, we present our conclusions.

II. DESCRIPTION OF THE MODEL

A. Introduction, definitions, and basic parameters

Generic optical displacement detection setups[15,19] are illustrated in Fig. 1. Here, the NEMS devices are probed through an objective lens by a tightly focused laser beam. The probe beam returning from the NEMS is collected by the same lens and is directed onto a photodetector. In Fabry-Perot interferometry [Fig. 1(a)], the power fluctuations in the probe beam are monitored as the NEMS moves. In path-stabilized Michelson interferometry [Fig. 1(b)], the probe beam interferes with a reference beam upon the photodetector. The parameters of the optical setup, which will be critical in setting up our models, are the numerical aperture (NA) and the focal length f of the objective lens. In the numerical computations that follow, we have set $f=4$ mm and NA $=0.5$, motivated by our experimental setup.[19] The selection of these values generates concrete numerical results without any loss of generality.
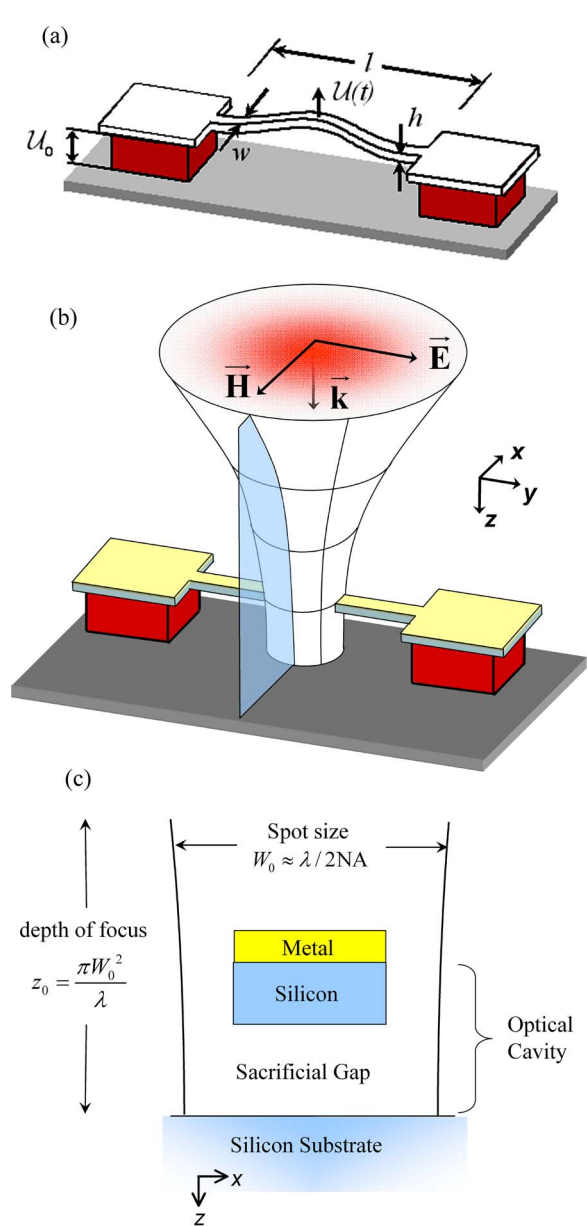

FIG. 2. (Color online) (a) The out-of-plane fundamental flexural mode of a doubly clamped beam. (b) The probe laser beam with Gaussian intensity profile and wave vector $\vec{k}$ is focused upon the center of the structure. The electric-field vector $\vec{E}$ is along the y axis and the magnetic field vector $\vec{H}$ is along x axis. (c) Finite element analysis of the electromagnetic field is performed in the cross-sectional xz plane of the bilayered NEMS device. An optical cavity is formed between the metal layer and the silicon substrate when the sacrificial layer is etched away to release the structure.

The medium the light travels in is characterized by its permeability μ and complex permittivity ε_c. In general, $\varepsilon_c = \varepsilon - i\sigma/\omega_l$, where ε is the permittivity and σ is the conductivity. μ, ε, and σ are dependent upon the wavelength λ or the frequency ω_l of the light. As usual, k is the wave number and $k=2\pi/\lambda$.

In this manuscript, we concentrate on NEMS in the doubly clamped beam geometry. Such doubly clamped beam resonators with dimensions $l \times w \times h$ are usually operated in their fundamental flexural modes. In optical displacement detection, one usually excites the out-of-plane flexural mode as shown in Fig. 2(a), where the beam center is displaced by

$\mathcal{U}(t)$ from its equilibrium position. For simplicity, we shall assume that the resonator is driven at a single frequency ω close to its resonance frequency ω_0, i.e., $\mathcal{U}(t) = u e^{i\omega t}$.

Most commonly,[6,15,17,19,30] NEMS beams are fabricated in silicon-on-insulator (SOI) heterostructures with metallization layers atop for electronic coupling. We shall focus on such structures and assume further that the metallization layers are thick enough to be optically nontransparent. For a Cr metallization layer, for instance, this corresponds to a thickness of ~15 nm.[19] A submicron optical cavity exists beneath this metallization layer. The cavity comprises of the vacuum gap and the silicon layer of the beam itself [see Fig. 2(b)]. We shall call the equilibrium vacuum gap as $\mathcal{U}_o$ [see Fig. 2(a)]. In general, this equilibrium gap is much greater than the amplitude of vibrations, i.e., $\mathcal{U}_o \gg u$.

Before we turn to the details of the model, we outline our approach. A Gaussian-profile probe beam is focused upon the NEMS and the resulting EM field in the NEMS *near field* is determined using finite element analysis. The scattered-reflected field is first collimated and then propagated to a photodetector in the *far field*—in essence, simulating the experiments. Finally, the EM field intensity of this probe beam incident upon the photodetector is converted into a current flow in the detection circuit. In the analysis of Fabry-Perot interferometry, the field intensity of the probe beam upon the photodetector is simply integrated and multiplied with the photodetector responsivity. In the analysis of Michelson interferometry, the field intensity is determined from the interference pattern formed by the probe beam and a reference beam.

B. Electromagnetic field in the NEMS near field

First, we turn to the details of the numerical analysis of the EM field in the vicinity of the NEMS. To simplify, we have formulated the problem in two dimensions and used the paraxial approximation where appropriate; we shall discuss the validity of these approximations below.

We start with a TE-polarized, collimated simple Gaussian beam propagating along the z axis, as shown in Fig. 2(b). This incoming laser beam is focused onto the NEMS device through the objective lens. The electric-field magnitude $E_y^{(0)}(x,z)$ of the normalized, focused Gaussian beam is given as

$$E_y^{(0)}(x,z) \approx A_0 \exp[-x^2/W^2(z)] \exp[-i\phi(x,z)]. \quad (1)$$

The phase $\phi(x,z)$ as well as the function $W(z)$ are uniquely determined by the f and the NA of the objective lens at a given λ. For completeness, we shall review these basic relations in Gaussian optics.[31] The first parameter to be defined is the beam waist W_0—obtainable directly from the lens parameters. The depth of focus z_0 follows as $z_0 = \pi W_0^2/\lambda$. The physical meanings of the parameters z_0 and W_0 are apparent from their respective definitions. Now, we can turn to the definitions of $\phi(x,z)$ and $W(z)$:
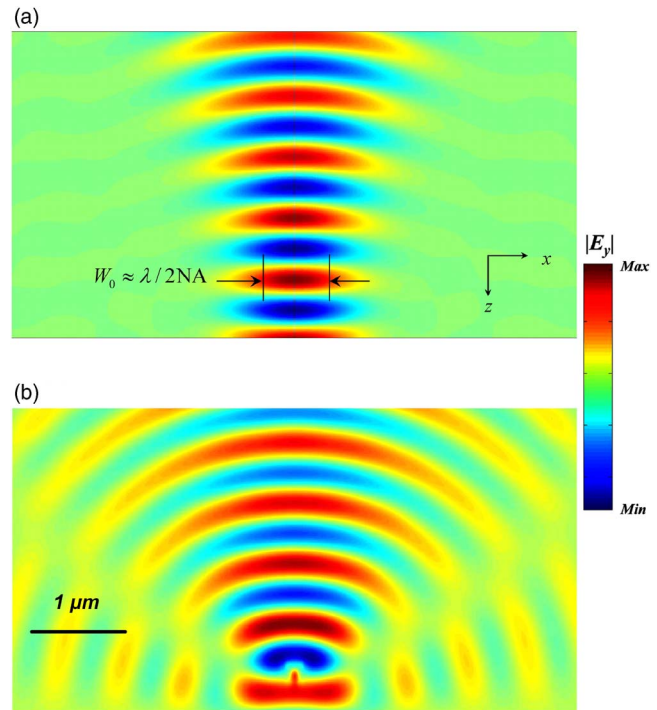
$$W(z) = W_0[1 + (z/z_0)^2]^{1/2}, \quad (2)$$

FIG. 3. (Color online) (a) A color plot of the electric-field amplitude $E_y^{(0)}(x,z)$ of the incoming Gaussian beam. Here, $\lambda = 632$ nm and the beam is focused by an objective lens of NA=0.5 and $f=4$ mm. (b) The electric-field amplitude $E_y^{(r)}(x,z)$ of the reflected-scattered EM field from a NEMS. The scattering NEMS beam has width $w=170$ nm, cavity length $\mathcal{U}_o=300$ nm, and silicon layer thickness $h=200$ nm (device not shown). This solution is obtained by finite element analysis. The substrate is positioned at the bottom in (b).

$$\phi(x,z) = kz + k\frac{x^2}{2z[1 + (z_0/z)^2]} - \tan^{-1}\frac{z}{z_0}. \quad (3)$$

In short, this operation creates the desired converging Gaussian with a radius of curvature $z[1 + (z_0/z)^2]$.

In experiments,[15,19] the Gaussian beam is focused upon the NEMS and the reflected light is collected by the focusing lens. This step is modeled by placing the NEMS at the focal point of the above-described converging Gaussian beam, as shown in Figs. 2(b) and 2(c). We determine the electric field by solving the time harmonic *vector* field equation[32] $\nabla \times (\nabla \times \mathbf{E})/\mu - \omega_l^2 \varepsilon_c \mathbf{E} = 0$ in the xz plane. We have used a finite element method to obtain the solution[33,34] in the vicinity of the NEMS. We then determine the reflected EM field by removing the incoming field profile given in Eq. (1). The reflected field amplitude is naturally a strong function of the x and z coordinates in the vicinity of the NEMS—in the Fresnel diffraction zone. In Fig. 3, we display an incoming wave at $\lambda = 632$ nm and a finite element solution of the scattered wave $E_y^{(r)}(x,z)$ for a beam width of $w=170$ nm, silicon layer thickness of $h=200$ nm, and vacuum gap of $\mathcal{U}_o = 300$ nm.

The dynamic solution, where the NEMS displaces in the out-of-plane direction as a function of time t, can be formulated in the same manner. The EM field reflecting from the NEMS structure is a function of its position $\mathcal{U}(t) + \mathcal{U}_o$ above the substrate. Since $\mathcal{U}_o$ is time independent and $u \ll \mathcal{U}_o$, the

field $E_y^{(r)}$ reflecting from the NEMS in motion will have the harmonic time dependence of the NEMS motion, i.e., $E_y^{(r)}(x,z,t) \approx E_y^{(r)}(x,z)e^{i\omega t}$.

Now, we discuss the validity of the above-mentioned approximations. First, we have modeled the EM field in two dimensions, i.e., in the xz plane [see Figs. 2(a) and 2(b)], which passes through the center of the nanomechanical beam. This is a valid approximation if $l \gg 2W_0$. For first generation NEMS, where l is several micrometers and $2W_0 \approx 1 \ \mu m$, this approximation holds well.[19] This approximation is expected be less accurate for large optical spot sizes or extremely small NEMS since the displacement will no longer be uniform within the optical spot. Second, we have used the paraxial approximation in modeling the Gaussian beam and its focusing through the lens. Paraxial approximation does not hold in high NA systems very accurately.[32] Beyond NA=0.7, our numerical models begin to display an asymmetry between the converging and diverging wave fronts as well as a shift in the focal point. We have verified that the Gaussian approximation is still acceptable for NA =0.5. Moreover, we have compensated for the focal point shifts when inserting the NEMS device into the model.

C. Propagation of the electromagnetic field

The next steps in our analysis are the collimation of the reflected beam through the objective lens and the free-space propagation of the collimated beam from the lens to the photodetector. These steps link the solution in the NEMS near-field region to the far-field photodetector.

To model the above steps, we have used Fourier optics. We have made an approximation in going from the (diffracted) EM field solution to Fourier analysis. We consider two important issues that have motivated this approximation. First, spatial frequencies in the EM field subject to Fourier analysis should not exceed the inverse wavelength $1/\lambda$.[32] Yet, our EM field solutions at the focal plane of the lens $E_y^{(r)}(x, z \approx 0)$ contain high spatial frequency fluctuations— due to the strong diffraction from the subwavelength NEMS. Experimentally, the lens collecting the scattered light filters out these high spatial frequencies.[35] Second, only the diffracted-reflected EM field with wave vector lying within the angle of convergence $\theta_0 \approx W_0/z_0$ of the lens can be collected (see Fig. 3). Mathematically, this can be expressed as the cone angle limit $-\theta_0 \leqslant \cos^{-1}(\hat{z} \cdot \hat{k}) \leqslant \theta_0$ between the unit vector $\hat{z}$ of the optical axis and the unit wave vector $\hat{k}$ of the reflected wave. We have circumvented both these issues by looking at the EM field solution $E_y^{(r)}(x,z)$ slightly above the focal plane at $z \sim 5\lambda$—where (i) the very high frequency fluctuations have died down, but the crucial features in the EM field due to the NEMS are present, and (ii) the solution possesses mostly the desired wave vectors. To simplify, we have assumed that this solution at $z \sim 5\lambda$ is approximately at the focal plane $z \approx 0$. For the lens parameters we are using, the depth of focus of the lens is $z_0 \approx \pi\lambda$, and this crucial assumption does not introduce a significant source of error.[36] For higher NA lenses, this approximation would not be valid.

We now turn to the inverse Fourier transform relation arising from the presence of the (collection-collimation) lens. The collimated electric field[37] at the observation plane at $z =f$ can be obtained as

$$E_y^{(c)}(x) \approx \frac{\exp[i(k/4f)x^2]}{(i\lambda f)^{1/2}} \int_{-\infty}^{\infty} dx' E_y^{(r)}(x') \exp\left[i\frac{2\pi}{\lambda f}(xx')\right].$$

(4)

Here, the integration is performed over the focal plane at $z =0$ of the lens with focal length f.

This collimated field $E_y^{(c)}(x)$ is then propagated in free space, along the optical axis (z axis). The electric field $E_y^{(p)}(x)$ at the photodetector, located at a distance $z=L$ from the collimation lens, can be represented as an integral of harmonic functions,[32]

$$E_y^{(p)}(x,z=L) = \int_{-\infty}^{\infty} F_{\text{col}}(\nu_x)\exp(-i2\pi\nu_x x)\exp(-ik_z L)d\nu_x.$$

(5)

Here, $F_{\text{col}}(\nu_x)$ is the Fourier transform of $E_y^{(c)}(x)$ with spatial frequency $\nu_x = k_x/2\pi$ and wave number k_x. The wave number along the axis of propagation is defined as $k_z = \sqrt{k^2 - k_x^2}$. Note that L is much greater than any length scale in the NEMS near field. We have used the definition in Eq. (5) to implement a fast Fourier transform (FFT) algorithm for free-space propagation. To prevent aliasing, beam propagation calculation is performed in incremental steps of $\Delta L \approx \lambda$ in an iterative manner. Spatial window of the discrete Fourier transform is picked large enough to avoid the edge effects associated with numerical FFT.

D. Detection circuit

As the final step, the optical power in the EM field returning from the NEMS is converted into a photodetector current I. Before we turn to the details of obtaining I, we shall introduce a useful parameter called the *optical reflectivity* R of a NEMS device. R is defined as the ratio of the reflected power to the incident power. The incident power P_0 is constant on any plane along the optical axis.[38] The total reflected power is the integrated intensity profile of the electric field $E_y^{(pd)}$ incident on the photodetector. Hence, the reflectivity can be expressed as an integral over the photodetector surface,

$$R = \frac{1}{P_0} \int_A \sqrt{\frac{\varepsilon_0}{\mu_0}} \frac{|E_y^{(pd)}|^2}{2} dA.$$

(6)

Using Eq. (6), the photodetector current can be expressed as $I = \Re_{\text{pd}} P_0 R$, where $\Re_{\text{pd}} = \eta e/\hbar \omega_l$ is the photodiode responsivity. Here, η is the quantum efficiency of the photodetector, e is the electronic charge, and $\hbar$ is Planck's constant. The constants ε_0 and μ_0 are the permittivity and the permeability of
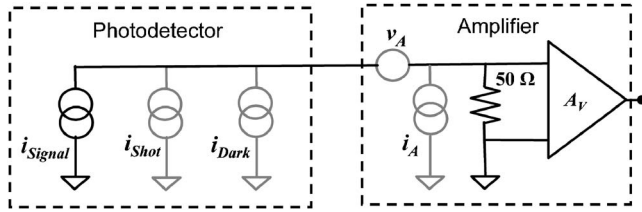
FIG. 4. The photodetector circuit model. The noise in the circuit arises from uncorrelated current and voltage sources shown in the lighter tone. The rf amplifier has a 50 Ω input impedance and two uncorrelated noise sources.
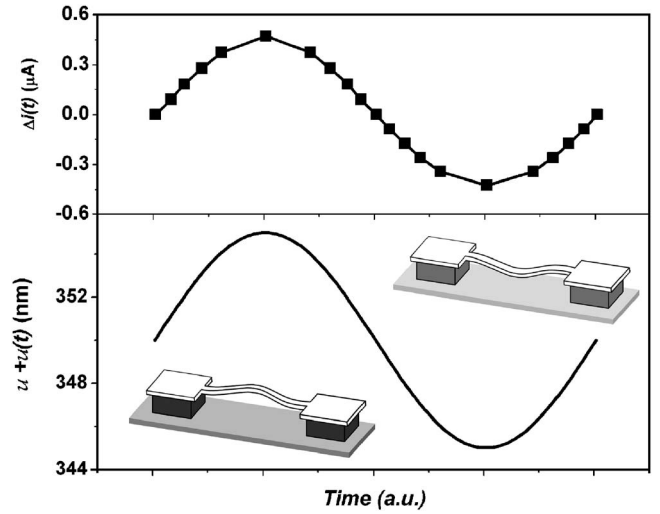

FIG. 5. The photodetector current (upper plot) calculated as a function of the beam position (lower plot) using the presented model. The following parameters are used: $w=170$ nm, $h=200$ nm, and $\mathcal{U}_o=350$ nm with a vibrational amplitude of $u=5$ nm. The current is calculated at the photodiode located at $L \approx 15$ cm from the sample. The detector responsivity is $\mathfrak{R}_{pd}=0.4$ A/W and the probing laser beam power is $P_0=100$ μW at $\lambda=632$ nm.

vacuum, respectively. For Fabry-Perot interferometry, the EM field incident on the photodiode is simply the propagated wave of Eq. (5), i.e., $E_y^{(pd)}=E_y^{(p)}$. Alternatively, Michelson interferometry can be simulated by interfering the propagated wave with a reference beam $E_y^{(ref)}$, i.e., $E_y^{(pd)}=E_y^{(p)}+E_y^{(ref)}$.

The noise model for the photodetector-amplifier circuit is presented in Fig. 4. The noise sources originating in the detection circuit are the shot noise and the dark current noise of the photodetector and the electronic noise of the amplifier. We shall express these various sources in terms of their equivalent current noise with power spectral density S_I (in units of A^2/Hz). The shot-noise power spectral density $S_I^{(S)}$ is given by $S_I^{(S)}=\mathfrak{R}_{pd}e\int_A \sqrt{\varepsilon_0/\mu_0}\langle|E_y^{(pd)}|^2\rangle dA$. The brackets denote the time-averaged value. The dark current with $S_I^{(D)}$ depends upon the reverse bias and the size of the active photodetector area.[32] The noise generated within the amplifier can be described by two uncorrelated noise sources: a voltage noise and a current noise source with power spectral densities $S_V^{(A)}$ and $S_I^{(A)}$, respectively, as shown in Fig. 4. In radio-frequency amplifiers, the input impedance $R_{in}=50$ Ω and hence the total noise can be converted into a noise current where $S_I^{(AT)} \leq S_I^{(A)}+S_V^{(A)}/R_{in}^2$. In a typical photodetector-amplifier circuit, at the low optical power levels (~ 100 μW) used in NEMS experiments,[19] $S_I^{(S)} \approx 1$ pA^2/Hz, $S_I^{(D)} \approx 10^{-3}$ pA^2/Hz, and $S_I^{(AT)} \approx 100$ pA^2/Hz.

E. Combined model and noise analysis

With all the elements in hand, we can approximate the transfer function for the optical measurement setup. This transfer function relates the NEMS displacement amplitude u to the resulting photodetector current I at the NEMS motion frequency ω. The finite element analysis determines the u dependence of the reflected EM field, the collimation and propagation calculations determine the field profile incident upon the photodetector, and finally, the detector responsivity relates the EM field intensity on the detector to the obtained current I.

In Fig. 5, we display a calculation of the photodetector current as a function of the beam center position upon the substrate using the complete model. Here, we employ the following values: $\mathfrak{R}_{pd}=0.4$ A/W, $w=170$ nm, $h=200$ nm, $\lambda=632$ nm, and incident laser power $P_0=100$ μW.

The combination of all the components of the model allows us to numerically determine the system responsivity to NEMS displacements as

$$\mathfrak{R}_u(\omega) = \left|\frac{\partial I}{\partial u}\right| = \mathfrak{R}_{pd}P_0 \left|\frac{\partial R}{\partial u}\right|. \tag{7}$$

$\mathfrak{R}_u(\omega)$ of the system can then be employed to establish the minimum detectable displacement signal. Following standard practice, we shall define the minimum detectable displacement for a signal-to-noise ratio of unity (SNR=1). The main sources of noise in the optical setup are due to the photodetector circuit (see above discussion in Sec. II D), the laser source, and the mechanical vibrations of the overall setup. The laser source exhibits intensity and phase fluctuations and $1/f$ noise.

In an effort to isolate the dominant noise source, we estimate the magnitude of each noise contribution. First, the mechanical vibrations of the overall optical setup are negligible at the high operation frequencies of NEMS. For low optical power levels in a typical laser source, the laser noise is estimated to be small as compared to the other noise sources in the photodetector circuit,[39,40] leaving the noise generated in the amplifier as the dominant source of noise.

In the following calculations, we have converted the current noise to a displacement noise (in units of m/$\sqrt{\text{Hz}}$), defined as

$$\sqrt{S_u} = \frac{\sqrt{S_I^{(AT)}}}{\mathfrak{R}_u}, \tag{8}$$

using the spectral density of the dominant noise source $S_I^{(AT)} \approx 100$ pA^2/Hz and assuming that SNR=1.

III. DISPLACEMENT DETECTION IN NEMS BASED UPON OPTICAL CAVITIES

We now apply the above-developed model to study the sensitivity limits of NEMS displacement detection based

upon optical cavities.[15,19] Clearly, there is a vast parameter space that can be explored; our emphasis will be upon the various device dimensions. The expectation is to help design a NEMS device that will enable ultrasensitive displacement detection. We shall look at the following dimensions: width w and thickness h of the beam and the sacrificial gap size (thickness) $\mathcal{U}_o$. The effects of the detection wavelength λ will also be examined. For each parameter investigated, we shall present a plot of R versus the parameter in question. We shall also determine the displacement responsivity of Fabry-Perot interferometry $\mathfrak{R}_u^{(FP)}$ and the displacement noise floor, where appropriate. For concreteness, we have used the typical values of $\mathfrak{R}_{pd}=0.4$ A/W and $P_0=100$ μW in these calculations.[41]

A. Optical cavity length

Figure 6 displays the effects of the sacrificial (vacuum) gap upon the optical characteristics of the device. The gap size $\mathcal{U}_o$ along with h essentially sets the length of the optical cavity. In Fig. 6(a), we present the reflected power from the cavity as $\mathcal{U}_o$ is varied for three different beams with w =170, 300, and 400 nm and h=200 nm at λ=632 nm. Apparently, the power is oscillating with $\mathcal{U}_o$ and the oscillations have a period of $\sim\lambda/2$, independent of w. This is consistent with a signal obtained from the interference of light reflected from the top of the nanomechanical beam and the substrate. The displacement responsivity $\mathfrak{R}_u$ introduced in Eq. (6) can be extracted by determining the rate of change of the photo-detector signal with respect to the cavity length. $\mathfrak{R}_u^{(FP)}$ as a function of $\mathcal{U}_o$ is presented in Fig. 6(b). By utilizing the dominant noise value $S_I^{(AT)}\approx100$ pA^2/Hz, the displacement sensitivity (noise floor) $\sqrt{S_u}$ can also be determined—as shown in Fig. 6(c).

B. Beam width and thickness

In our two-dimensional (2D) model, the width w of the NEMS beam essentially determines the reflectivity of the device. The effects of the beam width already manifest in the plots of Fig. 6. The maximum reflectivity value *does* vary with the beam width. In Fig. 7(a), we hold the vacuum gap and the beam thickness constant at $\mathcal{U}_o$=400 nm and h =200 nm, respectively; we vary the beam width w and determine the reflectivity of the device. We have performed this calculation for metallized silicon NEMS as well as for pure metal devices *for comparison*. A metallic device shows a monotonically decreasing R as the optical spot size becomes larger than the device—until all the light starts to reflect from the substrate. The metallized silicon, in contrast, exhibits a peak in R around $w\approx160$ nm. The slight increase in the device reflectivity below w=160 nm is possibly the result of an increase in the fraction of the power reflecting from the substrate.

In Fig. 7(b), we display the results of maximum displacement responsivity $\mathfrak{R}_u^{(FP-max)}$ as a function of w. For obtaining $\mathfrak{R}_u^{(FP-max)}$, we have generated plots similar to Fig. 6(b) for each w.
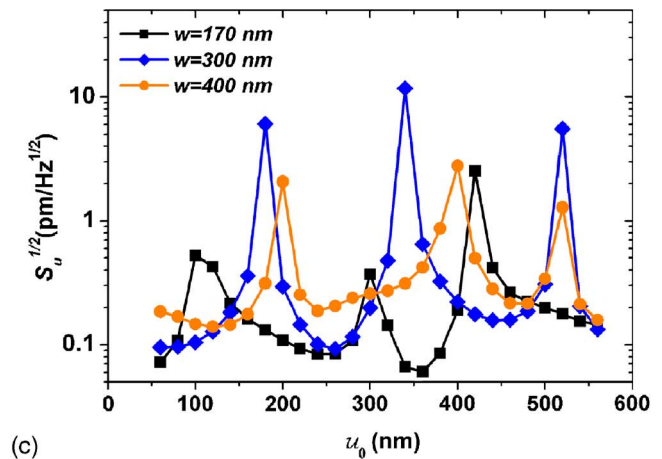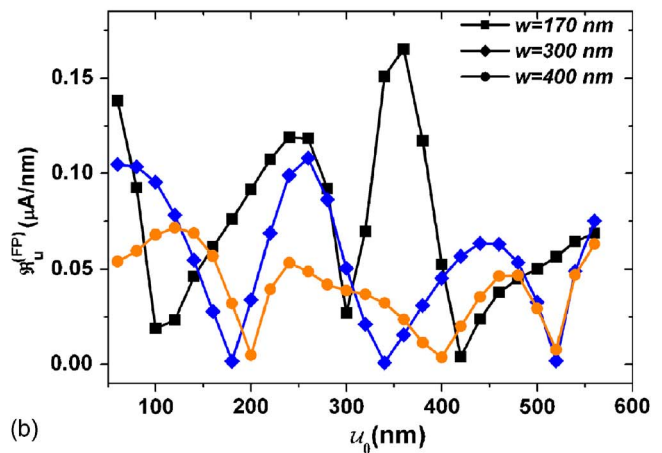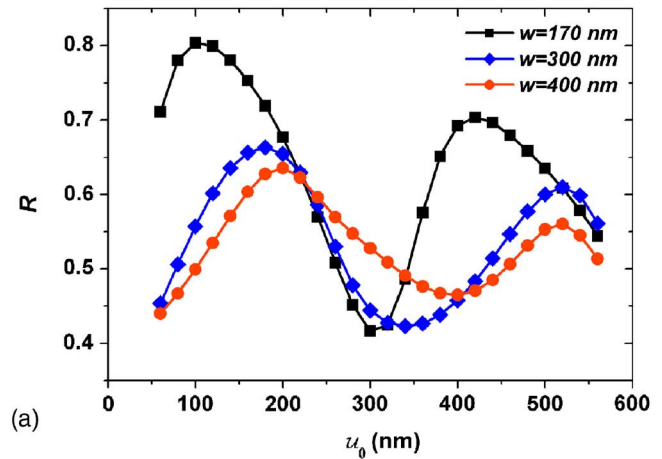

FIG. 6. (Color online) Optical characteristics of a set of NEMS beams with w=170, 300, and 400 nm and h=200 nm as a function of $\mathcal{U}_o$. The plots are for $P_0=100$ μW and $\mathfrak{R}_{pd}=0.4$ A/W. (a) Device reflectivity R oscillates with a period of $\sim\lambda/2$ as $\mathcal{U}_o$ is varied. Note that the oscillation amplitude of R is highest for the smallest structure. (b) Displacement responsivity $\mathfrak{R}_u^{(FP)}$ is the relevant quantity for displacement detection. It is calculated by numerically differentiating the data in (a) with respect to $\mathcal{U}_o$. (c) Displacement sensitivity results based upon $\sqrt{S_I}=10$ pA/$\sqrt{Hz}$.

C. Wavelength

The wavelength λ of the light is another parameter that we have studied. In these studies we have fixed the dimensions of the NEMS as well as the optical parameters such as
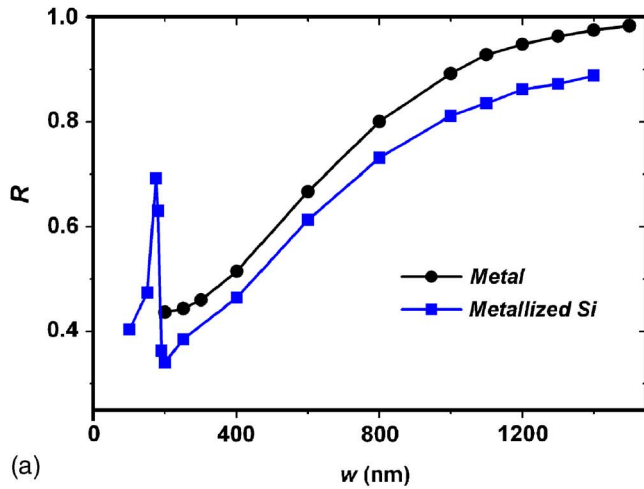
(a)
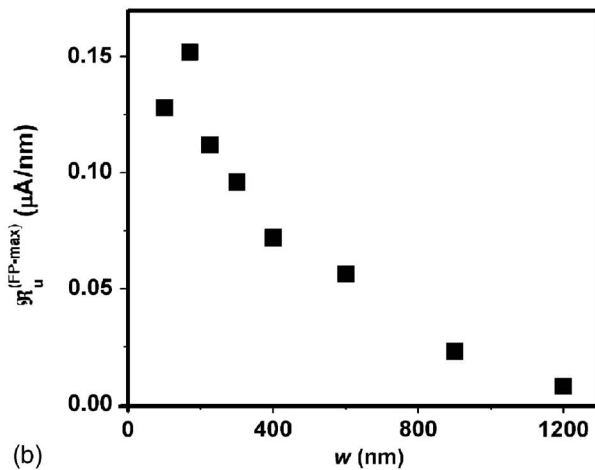
(b)

FIG. 7. (Color online) (a) Reflectivity as a function of the beam width for metallic and metallized silicon NEMS beams. Here, silicon layer thickness is set to $h = 200$ nm, and the gap thickness is set to $\mathcal{U}_o = 400$ nm. A cavity resonance appears to become dominant at $w \approx 160$ nm in the metallized silicon beams. (b) Maximum displacement responsivity $\mathfrak{R}_u^{(\text{FP—max})}$ of the Fabry-Pérot technique as a function of w.
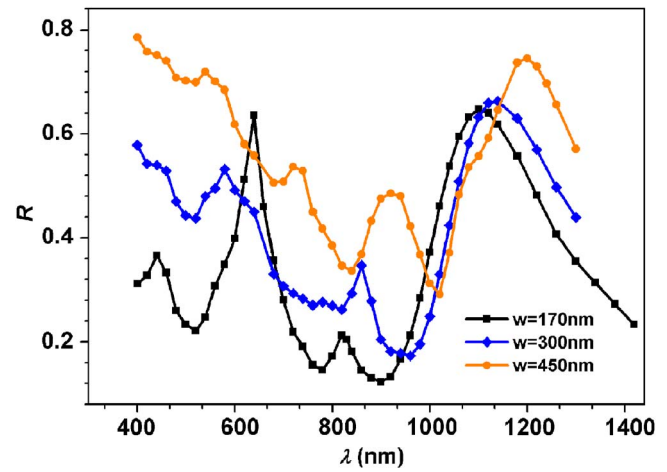

FIG. 8. (Color online) Device reflectivity R vs λ for three devices with width $w = 170$, 300, and 400 nm. Here, $h = 200$ nm, $\mathcal{U}_o = 350$ nm, and parameters of the free-space optics are kept constant for all the simulations.

$$\lambda_q = \frac{2\mathcal{U}_o^{(\text{eff})}}{q} \quad \text{for } q = 1, 2, 3 \ldots . \tag{9}$$

Here q is the axial mode number. The results in Fig. 8 for the $w = 170$ nm beam clearly show the expected resonances at their respective wavelengths, for mode number values of $q = 2$, 3, and 4 in the spectrum analyzed. In larger beam widths, such pronounced peaks are harder to locate. We speculate that this could be due to reduced power flow into the cavity as w is enlarged or due to increased losses in the material. In any case, the calculated optical quality factor F values are highest in the $w = 170$ nm beam approaching $F \approx 10$ at $\lambda \approx 640$ nm. As the beam width is increased at the same wavelength, F decreases to $F \approx 8$ for the $w = 450$ nm beam. Apparently, the quality factor values here are much lower than those reported in MEMS devices.[43]

the NA and f and investigated the optical response as a function of λ.

Cavity resonances of light have been studied and exploited for device characterization in microelectromechanical system[42] (MEMS) and in microscale optomechanical filters.[43] Here, we extend this analysis to subwavelength NEMS structures by employing a range of wavelengths from $\lambda \approx 400$ nm up to $\lambda \approx 1300$ nm in the above-described model. We note that optical properties of silicon vary significantly within this spectrum and we have taken great care in performing these calculations with the correct permittivity values.

The reflectivity values of the cavities in suspended silicon beams with $w = 170$, 300, and 400 nm, $\mathcal{U}_o = 400$ nm, and $h = 200$ nm are displayed in Fig. 8. Several resonances are apparent in each NEMS device. For these structures, the effective optical cavity length beneath the metal layer and the substrate, including the thickness h of the silicon layer, is $\mathcal{U}_o^{(\text{eff})} = \mathcal{U}_o + n_{\text{Si}}h$ [see Fig. 2(b)]. Simple optical path-length arguments suggest that optical resonances are expected at

IV. PATH-STABILIZED MICHELSON INTERFEROMETRY

Our discussion thus far has concentrated on Fabry-Perot interferometry in NEMS; yet, our model can be adjusted to analyze the displacement sensitivity of Michelson interferometry. To assess the effectiveness of Michelson interferometry in NEMS, cavity effects ought to be removed from the analysis. Physically, this corresponds to removing the substrate (see Figs. 2 and 3 above).[13]

The analysis of Michelson interferometry is essentially the same as the analysis of Fabry-Perot interferometry. The only difference is in the final step, where the EM field $E_y^{(p)}$ returning from the NEMS is interfered with a reference beam $E_y^{(\text{ref})}$. The reference beam can be defined as $E_y^{(\text{ref})} = |E_y^{(\text{ref})}| e^{-i\varphi_{\text{ref}}}$ with an arbitrary phase φ_{ref}, which can be adjusted by shifting the location of the reference mirror in the setup illustrated in Fig. 1(b) above. The intensity of the interference profile formed on the photodiode is proportional to $|E_y^{(p)} + E_y^{(\text{ref})}|^2$, which is expanded as
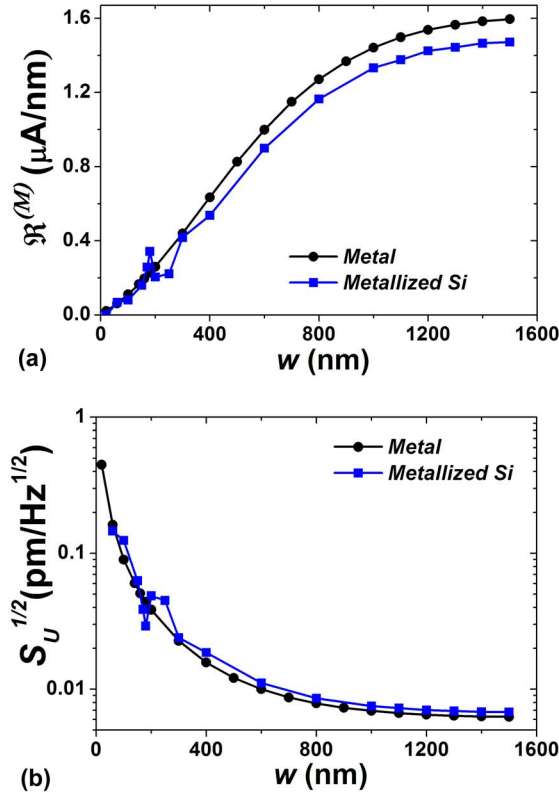
FIG. 9. (Color online) (a) The displacement responsivity $\mathfrak{R}_u^{(M)}$ and (b) noise floor of Michelson interferometry in NEMS. The back substrate is removed to eliminate any cavity effects. Here, $P_0 = 100$ μW at $\lambda = 632$ nm, $\sqrt{S_I} = 10$ pA/$\sqrt{\text{Hz}}$, and $\mathfrak{R}_{pd} = 0.4$ A/W.

$$|E_y^{(p)} + E_y^{(\text{ref})}|^2 \approx |E_y^{(p)}|^2 + |E_y^{(\text{ref})}|^2 + 2|E_y^{(\text{ref})}||E_y^{(p)}|\cos(\Delta\varphi). \tag{10}$$

Here, $\Delta\varphi$ is roughly the phase difference between the reference and probe beams and depends upon the NEMS position as well as φ_{ref}. The photodetector current in Michelson interferometry is, therefore, $I^{(M)} = \mathfrak{R}_{pd} \int_A \sqrt{\varepsilon_0/\mu_0} (|E_y^{(p)} + E_y^{(\text{ref})}|^2/2) dA$. Similar to Eq. (7) above, we define a displacement responsivity for small NEMS displacements as

$$\mathfrak{R}_u^{(M)}(\omega) \approx \left| \frac{\partial I^{(M)}}{\partial u} \right|. \tag{11}$$

In experiments, one usually adjusts φ_{ref} until a maximum responsivity is obtained; in our calculations, we normalize the obtained Michelson responsivity values to remove the effect of φ_{ref}.

$\mathfrak{R}_u^{(M)}$ and the displacement detection noise floor $\sqrt{S_u}$ for Michelson interferometry are shown in Figs. 9(a) and 9(b), respectively. This calculation is performed for pure metal beams and metallized silicon beams using the following parameters: $\mathcal{U}_o = 400$ nm, $h = 200$ nm, $\lambda = 632$ nm, $P_0 = 100$ μW, and $\mathfrak{R}_{pd} = 0.4$ A/W. We use the dominant noise source $S_I^{(AT)} \approx 100$ pA^2/Hz. The responsivity decreases and the noise floor increases as the reflecting surface of the NEMS beam is reduced below the diffraction-limited spot size. There appears to be an interesting resonance in the silicon beams. Given that the substrate is removed, we speculate that this resonance arises inside the silicon layer.

V. CONCLUSIONS

Here, we have developed a detailed numerical model to study optical displacement detection in NEMS. We have then used this model to elucidate the displacement sensitivity limits as a function of various device parameters, optical parameters, and interferometry type—in Figs. 6–9.

A first significant set of results concerns displacement detection in NEMS based upon cavities. Our results clearly indicate that devices with certain dimensions enable enhanced displacement detection. There are several avenues in which these results can be exploited to implement ultrasensitive displacement detection in NEMS. First, in the device design stage, one can select a SOI wafer with the appropriate layer thicknesses to enhance the response. Second, after design, one can tune the vacuum gap $\mathcal{U}_o$ by flexing the beam towards the substrate using electrostatic forces to obtain $\mathfrak{R}_u^{(\text{FP}-\text{max})}$. Finally, λ can be adjusted in the measurement stage to improve the optical response of the device.

The study of Michelson interferometry indicates that the displacement sensitivity of path-stabilized Michelson optical interferometry quickly deteriorates in the NEMS domain. $\mathfrak{R}_u^{(M)}$ decreases monotonically with decreasing beam width w, and there appears to be no exceptions to this general trend.

We conclude by reemphasizing that we have observed some of the above-described trends experimentally in recent measurements.[19] This clearly suggests that modeling will be extremely important in the design and operation of next generation optical NEMS devices.

[1] M. L. Roukes, Phys. World **14**, 25 (2001).
[2] H. G. Craighead, Science **290**, 1532 (2000).
[3] X. M. H. Huang, C. A. Zorman, M. Mehregany, and M. L. Roukes, Nature (London) **421**, 496 (2003).
[4] A. N. Cleland and M. L. Roukes, Nature (London) **392**, 160 (1998).
[5] L. Sekaric, M. Zalalutdinov, S. W. Turner, A. T. Zehnder, J. M. Parpia, and H. G. Craighead, Appl. Phys. Lett. **80**, 3617 (2002).
[6] A. Erbe, H. Krömmer, A. Kraus, R. H. Blick, G. Corso, and K. Richter, Appl. Phys. Lett. **77**, 3102 (2000).
[7] K. L. Ekinci, X. M. H. Huang, and M. L. Roukes, Appl. Phys. Lett. **84**, 4469 (2004).
[8] B. Ilic, H. G. Craighead, S. Krylov, W. Senaratne, C. Ober, and P. Neuzil, J. Appl. Phys. **95**, 3694 (2004).
[9] N. V. Lavrik and P. G. Datskos, Appl. Phys. Lett. **82**, 2697 (2003).
[10] A. Gupta, D. Akin, and R. Bashir, Appl. Phys. Lett. **84**, 1976 (2004).
[11] K. C. Schwab, E. A. Henriksen, J. M. Worlock, and M. L. Roukes, Nature (London) **404**, 974 (2000).
[12] C. S. Yung, D. R. Schmidt, and A. N. Cleland, Appl. Phys. Lett. **81**, 31 (2002).

[13]M. D. LaHaye, O. Buu, B. Camarota, and K. C. Schwab, Science **304**, 74 (2004).

[14]R. Knobel and A. C. Cleland, Nature (London) **424**, 291 (2003).

[15]D. W. Carr, L. Sekaric, and H. G. Craighead, J. Vac. Sci. Technol. B **16**, 3821 (1998).

[16]D. W. Carr, S. Evoy, L. Sekaric, A. Olkhovets, J. M. Parpia, and H. G. Craighead, Appl. Phys. Lett. **77**, 1545 (2000).

[17]C. Meyer, H. Lorenz, and K. Karrai, Appl. Phys. Lett. **83**, 2420 (2003).

[18]B. E. N. Keeler, D. W. Carr, J. P. Sullivan, T. A. Friedmann, and J. R. Wendt, Opt. Lett. **29**, 1182 (2004).

[19]T. Kouh, D. Karabacak, D. H. Kim, and K. L. Ekinci, Appl. Phys. Lett. **86**, 013106 (2005).

[20]G. G. Yaralioglu, A. Atalar, S. R. Manalis, and C. F. Quate, J. Appl. Phys. **83**, 7405 (1998).

[21]M. G. L. Gustafsson and J. Clarke, J. Appl. Phys. **76**, 172 (1994).

[22]C. A. J. Putman, B. G. De Grooth, N. F. Van Hulst, and J. Greve, J. Appl. Phys. **72**, 6 (1992).

[23]T. R. Albrecht, P. Grütter, D. Rugar, and D. P. E. Smith, Ultramicroscopy **42**, 1638 (1992).

[24]W. Allers, A. Schwarz, U. D. Schwarz, and R. Wiesendanger, Rev. Sci. Instrum. **69**, 221 (1998).

[25]H. J. Hug, B. Stiefel, P. J. A. van Schendel, A. Moser, S. Martin, and H.-J. Güntherodt, Rev. Sci. Instrum. **70**, 3625 (1999).

[26]J. W. Wagner, Phys. Acoust. **19**, 201 (1990).

[27]D. S. Marx and D. Psaltis, J. Opt. Soc. Am. A **14**, 6 (1997).

[28]X. Wang, J. Mason, M. Latta, D. Marx, and D. Psaltis, J. Opt. Soc. Am. A **18**, 3 (2001).

[29]W. C. Liu and M. W. Kowarz, Appl. Opt. **38**, 17 (2003).

[30]D. W. Carr, S. Evoy, L. Sekaric, H. G. Craighead, and J. M. Parpia, Appl. Phys. Lett. **75**, 920 (1999).

[31]A. Yariv, *Quantum Electronics* (Wiley, New York, 1989).

[32]B. E. A. Saleh and M. C. Teich, *Fundamentals of Photonics* (Wiley, New York, 1991).

[33]J. Jin, *The Finite Element Method in Electromagnetics* (Wiley, New York, 1993).

[34]For this, the domain is meshed into triangular, quadratic Lagrange-type elements of maximum edge lengths less than a tenth of the effective wavelength $\lambda_{effective} = \lambda/|n_c|$ in order to keep the numerical noise below 1%. Here, $n_c = \sqrt{\varepsilon_c/\varepsilon_0}$ is the complex refractive index. The discretized problem is solved by harmonic propagation analysis using a stationary, direct solver; FEMLAB Electromagnetics Module User Guide, Comsol, Inc., Burlington, MA, 2004.

[35]C. Triger, C. Ecoffet, and D. J. Lougnot, J. Phys. D **36**, 2553 (2003).

[36]We have extracted the reflected wave from EM solutions at different planes $z \approx \lambda$, 2λ, 3λ, 4λ, and 5λ for a specific finite element model and carefully compared the resulting intensity profiles at the photodetector. Our results indicate that the collimated profile variation is negligible between the solutions sampled at different planes.

[37]J. W. Goodman, *Introduction to Fourier Optics* (McGraw-Hill, New York, 1996).

[38]Collimation lens is assumed to be lossless and therefore probing laser power does not change from the collimation plane to the focal plane.

[39]K. Petermann, *Laser Diode Modulation and Noises* (Kluwer Academic, Dordrecht, 1988).

[40]The laser noise, when converted to a current noise on the photodetector, has power $S_I^{(L)} \approx 1$ pA^2/Hz.

[41]It is possible to scale all the relevant data by incident laser power P_0 and the photodetector responsivity $\mathfrak{R}_{pd}$.

[42]T. H. Stievater, W. S. Rabinovich, H. S. Newman, J. L. Ebel, R. Mahon, D. J. McGee, and P. G. Goetz, J. Microelectromech. Syst. **12**, 1 (2003).

[43]R. S. Tucker, D. M. Baney, W. V. Sorin, and C. F. Flory, IEEE J. Sel. Top. Quantum Electron. **8**, 1 (2002).